Research Article

Wanming Li, Ximin Zang*, Haiyang Qi, Dejun Li, and Xin Deng

Research on the ingot shrinkage in the electroslag remelting withdrawal process for 9Cr3Mo roller

https://doi.org/10.1515/htmp-2019-0014
Received Oct 02, 2018; accepted Dec 25, 2018

Abstract: In order to reduce the air gap between ingot and mould in the electroslag remelting withdrawal (ESRW) process, the taper of the mould should be consistent with the ingot shrinkage. A three-dimensional mathematical model was developed to describe the interaction of multiple-physical fields (Joule heat, electromagnetic field, velocity field, and temperature field) and ingot shrinkage during the ESRW process. The variations of material thermal and mechanical properties, as well as the yield function with temperature, were considered. The shrinkage behavior of 9Cr3Mo roller in the ESRW process was simulated using the sequential coupling method. A good agreement between the calculated value and the measured value was obtained in the temperature field and stress field. Numerical results showed that maximum values of current density, Joule heat, and electromagnetic force were at the electrode corner of the slag bath. The direction of the magnetic flux density was tangential to the slag bath and had a clockwise rotation. There were two pairs of vortices and two high temperature zones in the slag bath. The shrinkage displacement was obtained through thermal-stress analysis. As the distance from the mould outlet decreases, the shrinkage displacement of ingot increases. As for the electroslag remelting withdrawal process for 9Cr3Mo roller, the variation of the shrinkage displacement from the slag/metal interface to the mould outlet was 0.0028 m. The maximum shrinkage displacement is at the mould outlet, and the value was 0.0089 m.

Keywords: ESRW; air gap; temperature field; ingot shrinkage; mould taper

1 Introduction

Electroslag remelting (ESR) products are characterized by compact structure, uniform composition and superior purity. The products are widely used in the aerospace, chemical, and energy industries, as well as for military and other applications [1]. Compared with the traditional ESR, the electroslag remelting withdrawal (ESRW) process has many advantages, such as increased productivity, yield, and decreased cost. Because of the large temperature gradient in the ESR process, there is an air gap between the ingot and the mould, which affects heat transfer of the ingot in the mould. In order to reduce the air gap, an inverted taper should be used [2]. If the mould taper is not suitable, the process would not proceed efficiently. If the inverted taper is too small, the heat transfer of the ingot will slow down, and if the taper is too large, the ingot will be difficult to demould. Leakage of molten steel and slag can also occur in serious cases when the taper is large [3]. The hydrostatic pressure of liquid steel acts vertically on the slag film during the ESRW process. Under normal circumstances, a slag film with molten steel wrapped inside is close to the inner wall of the mould, and the slag film will not be broken due to the internal support of the mould. However, if the taper is not reasonable, the air gap between the ingot and the mould will become larger under the action of ingot shrinkage. When the air gap extends upward to initial solidification shell near the slag-steel interface, the slag film will be crushed under the action of hydrostatic pressure of liquid steel, resulting in the leakage of steel and slag. Thus, the optimum design of the mould taper should be consistent with the volume change during ingot shrinkage. Therefore, it is important to study ingot shrinkage to develop ways to optimize the taper and minimize the leakage of molten steel and slag. As the requirement on product quality becomes more and stringent steadily, more detailed and precise approaches to the production technology should be adopted.

The temperature field is the basis of study for ingot shrinkage in the ESRW process. It is not possible to observe the melting and solidification process at the scene. A repeated trial and error method is very inefficient and expen-

***Corresponding Author: Ximin Zang:** School of material and metallurgy, University of Science and Technology Liaoning, Anshan, Liaoning 114051, China; Email: zangximin@163.com
Wanming Li, Haiyang Qi, Xin Deng: School of material and metallurgy, University of Science and Technology Liaoning, Anshan, Liaoning 114051, China
Dejun Li: State Key Laboratory of Marine Equipment and Applications, Anshan, Liaoning, 114051 China

sive, so it is not suitable for system studies in ESR [4]. The numerical simulation method is a more effective method for studying the temperature field. In order to obtain an accurate temperature field, it is necessary to study Joule heat, the electromagnetic field, and the velocity field in the ESRW process. Many scholars have studied various mathematical models using the traditional ESR process. A. Kharicha *et al.* [5] and E.Karimi Sibaki *et al.* [6] described the effect of current variation in the ESR process, but their model is a two-dimensional (2D) numerical model, so the accuracies of the simulation results were constrained. Li *et al.* [7] built a three-dimensional (3D) finite element model, considering the skin effect of alternating current (AC), but only the electromagnetic field and Joule heat were simulated and analyzed. In order to make the results more realistic, some scholars [8–12] considered the effect of droplet dripping in the ESR process. However, the study of the ingot shrinkage and mould taper design based on 3D multiphysics field distribution is rarely reported in the ESR process.

The numerical simulation of the ingot shrinkage in a 2D continuous casting mould has become mature, but no one has studied the 3D numerical model of ingot shrinkage in the ESRW process. Thomas *et al.* [13] developed a CON2D finite element model, using the elastic-viscoplastic creep constitutive equation to calculate the stress field both inside and outside of ingot in continuous casting mould. Koric [14] calculated the temperature field and stress field of the billet using two different elastomeric constitutive models. Some scholars [15, 16] studied the solidification shrinkage of molten steel in moulds. Cai *et al.* [17, 18] established a transient model of solidification heat transfer and elastic-plastic stress for 2D molten steel using the ANSYSTM software, and the deformation of steel was simulated by the indirect coupling method.

In our research, we developed a three-dimensional numerical model for multiple-physical fields (Joule heat, electromagnetic field, velocity field, and temperature field) and ingot shrinkage in the ESRW process for 9Cr3Mo roller. The multiple-physical fields and ingot shrinkage in the ESRW process were calculated using ANSYS finite-element analysis (FEA) software and computational fluid dynamics (CFD) software, including the consideration of the effect of metal droplets on the process. The ingot shrinkage rule in the mould of the ESRW process was analyzed by shrinkage displacement of ingot, which provides a theoretical basis for solving the problem of leakage of molten steel and slag.

2 Numerical Model

2.1 Geometric model

In our research, the electroslag remelting withdrawal process of 9Cr3Mo roller steel was simulated. The slag composition used in the ESRW process is 60% CaF_2, 20% CaO, and 20% Al_2O_3. The diagram of the ESRW process is shown in Figure 1. The process includes a consumable electrode, a slag bath, a liquid metal pool, a solidified ingot, and a mould. In order to simplify the calculations, the geometric model is simplified and the grid model is shown in Figure 2. The geometrical properties, specific process pa-

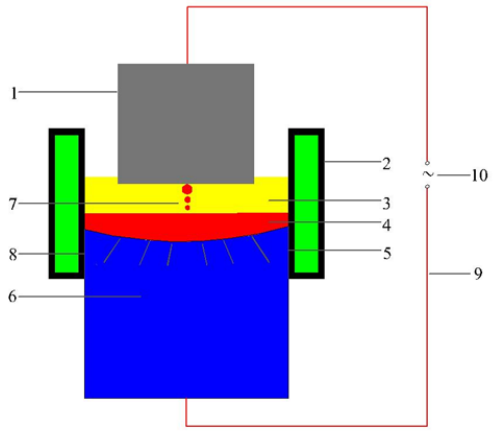

1. Electrode; 2. Mould; 3. Slagbath; 4. Metalmoltebath; 5. Slag skin; 6. Ingot; 7. Molten drops; 8. Air gap; 9. Wire; 10. Transformer

Figure 1: Principle diagram of ESRW process

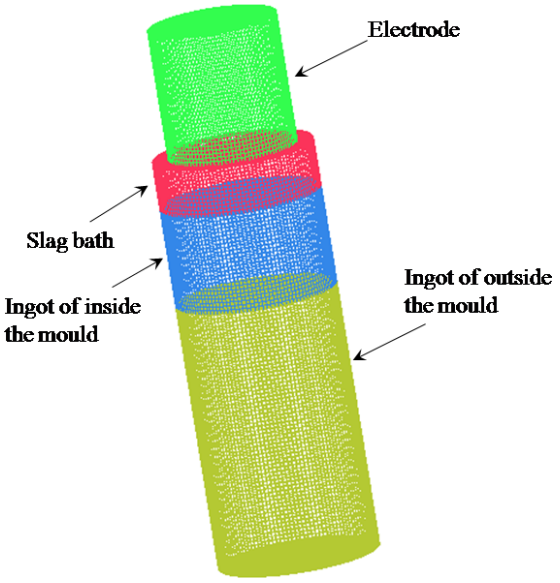

Figure 2: Grid model of the calculation domain

Table 1: Geometrical properties, operating conditions, physical properties of the ESRW system

Parameter			Value		
Geometry					
Electrode (diameter / height), m			0.48/0.5		
Electrode immersed depth, m			0.01		
Ingot diameter, m			0.6		
Ingot inside mould height, m			0.37		
Ingot outside mould height, m			1		
Slag (diameter / height), m			0.6/0.18		
Operating conditions					
Current amplitude, A			16500		
Frequency, Hz			50		
Physical properties of metal					
Density, $kg{\cdot}m^{-3}$			7800		
Specific heat, $J{\cdot}kg^{-1}{\cdot}K^{-1}$			753		
Thermal conductivity, $W{\cdot}m^{-1}{\cdot}K^{-1}$	781 K	1344 K	1572 K	1673 K	1723 K
	24.18	29	31.18	31.81	30.51
Electric conductivity, $\Omega^{-1}{\cdot}m^{-1}$			7.14×10^{5}		
Latent heat of fusion, $KJ{\cdot}Kg^{-1}$			267.1		
Liquidus / solidus, K			1564/1727		
Magnetic permeability, $H{\cdot}m^{-1}$			1.26×10^{-6}		
Elasticity modulus, GPa	573 K	873 K	1423 K	1679 K	1732 K
	209	178.6	71.32	2.8	2.4
Coefficient of linear expansion	576 K	986 K	1191 K	1421 K	1667 K
	1.3×10^{-5}	1.4×10^{-5}	1.1×10^{-5}	1.3×10^{-5}	1.5×10^{-5}
Poisson ratio	576 K	1911 K	1625 K	1653 K	1676 K
	0.2759	0.2759	0.2868	0.2998	0.3199
Yield stress, GPa	523 K	1173 K	1423 K	1639 K	1679 K
	0.019	0.018	0.007	0.003	0.0003
Physical properties of slag					
Density, $kg{\cdot}m^{-3}$			2594		
Specific heat, $J{\cdot}kg^{-1}{\cdot}K^{-1}$			837		
Thermal conductivity, $W{\cdot}m^{-1}{\cdot}K^{-1}$			10.46		
Liquidus, K			1668		
Thermal expansion coefficient, K^{-1}			1×10^{-4}		
Magnetic permeability, $H{\cdot}m^{-1}$			1.26×10^{-6}		
Viscosity, $Pa{\cdot}s^{-1}$	1623 K	1673 K	1723 K	1773 K	1823 K
	0.0369	0.0225	0.0202	0.018	0.0178
Electric conductivity, $\Omega^{-1}{\cdot}m^{-1}$	1723 K	1773 K	1823 K	1973 K	
	166.4	200.9	240	275	

rameters, and physical parameters of materials are shown in Table 1.

2.2 Basic assumptions

In order to make the simulation more accurate and efficient, the following assumptions were made:

(1) The ESRW process is a quasi-steady state.
(2) The slag/metal interface of the ESRW is horizontal.
(3) The thermal physical properties of the slag and ingot are related only to temperature.
(4) The heat of the molten droplets is generated by the internal heat source.

(5) Neglecting the influence of creep, the thermal stress analysis of the steel ingot is carried out by using the thermo-elastic-plastic model.
(6) The high temperature mechanical properties of the ingot are related only to temperature.

2.3 Governing equation

2.3.1 Equations for the electromagnetic field

The current density distribution is calculated using Ampere's law, where the current displacement is ignored:

$$\nabla \times H = J \tag{1}$$

$$\nabla \cdot B = 0 \tag{2}$$

$$\nabla \cdot J = 0 \tag{3}$$

$$B = \mu_a H \tag{4}$$

The current density is determined by Ohm's law:

$$J = \sigma E \tag{5}$$

The potential distribution equation is:

$$\nabla \cdot (\sigma \nabla \phi_k) = 0 \tag{6}$$

The Lorentz force and Joule heating therefore are described:

$$Q = \frac{J \cdot J}{\sigma} \tag{7}$$

$$F = J \times B = \mu_a J \times H \tag{8}$$

where H is the magnetic field intensity; J is the current density; B is the magnetic flux density; μ_a is the magnetic permeability of free space; σ is the electrical conductivity; E is the electric field intensity; φ_k is the potential; Q is the Joule heating; F is the Lorentz force.

2.3.2 Fluid-flow equations

The continuity equation and the Navier-Stokes equations can describe the flow phenomena in the slag pool as follows:

$$\nabla \cdot v = 0 \tag{9}$$

$$\rho_h (v \cdot \nabla) v = -\nabla P + \nabla \cdot \left(\mu_{eff} \cdot \nabla v\right) + F \tag{10}$$

The effective viscosity is the sum of molecular viscosity and turbulent viscosity, then:

$$\mu_{eff} = \mu + \mu_t \tag{11}$$

The turbulent viscosity can be calculated, by the following $\kappa - \varepsilon$ equations:

Turbulent kinetic energy κ satisfies the equation:

$$\rho_h \frac{\partial (\kappa v_j)}{\partial x_j} = \frac{\partial}{\partial x_j}\left(\frac{\mu_{eff}}{\sigma_\varepsilon}\frac{\partial \kappa}{\partial x_j}\right) + G - \rho\varepsilon \tag{12}$$

Turbulent dissipation rate ε satisfies the equations:

$$\rho_h \frac{\partial (\varepsilon v_j)}{\partial x_j} = \frac{\partial}{\partial x_j}\left(\frac{\mu_{eff}}{\sigma_\varepsilon}\frac{\partial \varepsilon}{\partial x_j}\right) + \frac{\varepsilon}{\kappa}(C_1 G - C_2 \rho\varepsilon) \tag{13}$$

$$G = \mu_t \frac{\partial v_i}{\partial x_j}\left(\frac{\partial v_i}{\partial x_j} + \frac{\partial v_j}{\partial x_i}\right) \tag{14}$$

The relation of turbulent viscosity μ_t to κ, ε can be described as:

$$\mu_t = \rho_h C_\mu \frac{\kappa^2}{\varepsilon} \tag{15}$$

where ρ_h is the density of molten; v is the velocity vector; P is the pressure; μ_{eff} is the effective viscosity of molten-metal; F is the body force; μ_t is the turbulent viscosity; C_1, C_2 are constant in the $\kappa - \varepsilon$ model; G is the generation term for turbulent kinetic energy; σ_κ, σ_ϵ are the Prandtl Numeral for the equation of κ and ϵ; C_μ is the dissipation rate constant. The model constants were assigned the values proposed by Launder and Spading [19].

2.3.3 Heat transfer equations

The heat transfer equation for the slag bath as follows:

$$\rho_h C_p (v \cdot \nabla T) = \nabla \cdot k_{eff} \nabla T + Q \tag{16}$$

Because the flow phenomenon of a metal molten bath is very complex, heat transfer of the bath can be simplified as conduction heat transfer, and the heat-transfer phenomenon can be described by an effective heat-transfer coefficient. The heat-conduction equation can be described as:

$$\rho_d C_{Pd} v_z \frac{\partial T}{\partial z} = \lambda_d \left(\frac{\partial^2 T}{\partial x^2} + \frac{\partial^2 T}{\partial y^2} + \frac{\partial^2 T}{\partial z^2}\right) + q_d \tag{17}$$

Where C_p is the heat capacity at a constant pressure; k_{eff} is the effective thermal conductivity of the slag pool; Q is the joule heat generated by the current; λ_d is the coefficient of thermal conductivity; v_z is the drawing speed; d stands for different regions, and $d = l, m, s$, where l is the metallic bath, m is the mushy zone, and s is the solidified ingot.

2.3.4 The thermo-elastic-plastic constitutive equations

The plastic processing is quite complicated in the thermo-elastic-plastic model. When the ingot enters the plastic state, there is no one-to-one correspondence between stress and strain. Strain not only depends on the current stress state, but it also depends on the entire loading history. It is impossible to establish the full relationship between the final stress and the strain, so the incremental theory must be used to establish the incremental relationship between stress and strain that is reflected in the loading history [20].

Considering the influence of temperature and strain rate, the total strain increment from the elastic-plastic theory is

$$\{d\varepsilon\} = \{d\varepsilon_e + d\varepsilon_p + d\varepsilon_\theta\} \tag{18}$$

Where ϵ is the total strain; ϵ_e is the elastic strain; ϵ_p is the plastic strain; ϵ_θ is the thermal strain.

The elastic strain obeys Hook's law. Considering the changes in the material parameters with temperature and strain rate, the incremental form is

$$\{d\varepsilon_e\} = [D_e]^{-1}\{d\sigma\} + \frac{\partial[D_e]^{-1}}{\partial\theta}\{\sigma\}\,d\theta + \frac{\partial[D_e]^{-1}}{\partial\dot{\varepsilon}}\{\sigma\}\,d\dot{\varepsilon} \tag{19}$$

According to the plastic flow rule of correlation, the plastic strain increment is

$$\{d\varepsilon_p\} = d\lambda\left\{\frac{\partial F}{\partial\sigma}\right\} \tag{20}$$

The thermal strain increment is

$$\{d\varepsilon_\theta\} = \{\alpha\}\,d\theta \tag{21}$$

Similarly, the yield function F should also consider the effects of temperature, strain rate, and the work hardening parameter K. The mathematical expression is

$$F = F(\{\sigma\}, K, \theta, \dot{\varepsilon}) \tag{22}$$

2.4 Calculation method and boundary conditions

2.4.1 Calculation method

Based on the size of the electroslag furnace, a three-dimensional (3D) geometric model was developed. The finite element mesh is divided by the mapping principle. According to the mathematical model and the process parameter table, the boundary conditions and initial conditions are applied to the whole system. The current density and Joule heat distribution of the whole system are calculated by thermoelectric coupling analysis unit (solid 69). The calculation results for the current density are introduced into the electromagnetic analysis unit (solid 97) to calculate the magnetic flux density and the electromagnetic force distribution of the whole system. Finally, the Joule heat is taken as the heat source and the electromagnetic force is taken as the driving force into the ANSYS CFX program. Using the CFX fluid-solid conjugate heat transfer module and the standard k-ϵ model, the velocity field and the temperature field are calculated. In the calculation of the stress analysis, the simulated ingot temperature field results are introduced into the thermal stress analysis unit. The ingot is subjected to thermal stress analysis. The flow chart of the calculation method is shown in Figure 3.

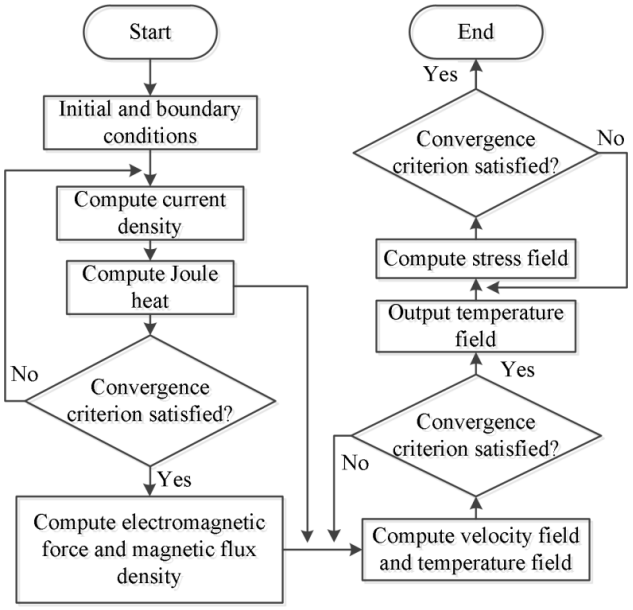

Figure 3: The flow chart of the calculation method

2.4.2 Electromagnetism and fluid flow

A consumable electrode is introduced into the current, and the bottom of the ingot is defined as zero potential. The magnetic induction intensity of the ESRW system is restrained. The slag/electrode interface, the slag bath side wall, and the slag/metal interface have no-slip boundary conditions. The slag /air interface has a free slip boundary condition.

2.4.3 Heat transfer and thermal stress

The consumable electrode is immersed in the slag bath as the liquidus temperature of the electrode. Radiation heat transfer and convective heat transfer between the slag bath and the air are simplified to the effective thermal conductivity.

The heat transfer between the slag pool and the mould conformed to the following equation:

$$q_{con} = h_{con}(T - T_w) \tag{23}$$

The heat transfer of the ingot surface in the mould conformed to the following equation:

$$k_e \frac{\partial T}{\partial x} = h_{cov}(T - T_w) \tag{24}$$

The heat transfer of the outside ingot surface of the mould conformed to the following equation:

$$k_e \frac{\partial T}{\partial y} = h_{oc}(T - T_c) \tag{25}$$

The thermal conductivity of the outside ingot surface of the mould is divided into two parts, convective heat conduction and radiant heat conduction:

$$h_{oc} = h_{oca} + h_{ocb} \tag{26}$$

Where h_{con} is the thermal conductivity between the slag bath and the mould; k_e is the thermal conductivity of the ingot; h_{cov} is the comprehensive thermal conductivity between the ingot side and the mould.

The heat-transfer boundary conditions used in the model are as follows. The heat transfer coefficient between the air and the electrode was 25.1 $W{\cdot}m^{-1}{\cdot}K^{-1}$. The heat transfer coefficient between the air and slag was 985 $W{\cdot}m^{-1}{\cdot}K^{-1}$. The heat transfer coefficient at the side of the slag bath was 1352 $W{\cdot}m^{-1}{\cdot}K^{-1}$. With increasing distance between the slag/metal interface and the outlet of the mould, the heat transfer coefficient of ingot sides decreased linearly from 271 to 8 $W{\cdot}m^{-1}{\cdot}K^{-1}$. The ingot sides outside the mould was 6 $W{\cdot}m^{-1}{\cdot}K^{-1}$ [21]. The metal material obeyed the Von Mises yield criterion, and the ingot surface was a free surface.

3 Simulation results analysis and validation

3.1 Electromagnetic field and Joule heat

Figure 4 shows the potential distribution of the longitudinal section in the ESRW. Because the slag bath is the largest resistance, most of the voltage-drop occurs in the slag bath. The electrode immersed in the slag bath has the largest potential gradient. The potential of the slag/metal interface approached zero.

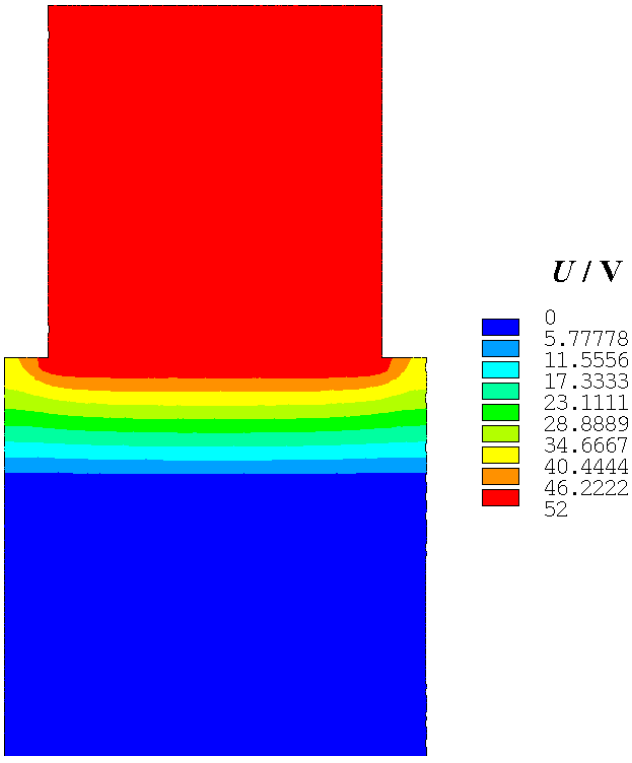

Figure 4: The potential distribution of longitudinal section of the ESRW

Figure 5 shows the current density distribution of the longitudinal section in the ESRW. The current flows into the electrode and flows out of the ingot from top to bottom. The current density distribution in the electrode and ingot area is more regular. Because the electrical conductivity of the slag bath is much less than for the electrode and ingots, the current density changes rapidly in the slag bath. When the current flows into the slag bath, it is redistributed. The current density of the electrode corner in the slag bath has the highest value of 378078 $A{\cdot}m^{-2}$. Figure 5 also verifies the distribution of the potential in the slag pool. Therefore, the electrode corner is the main heating zone for the electrode melting in the slag bath.

Figure 6 shows the Joule heat distribution in the slag bath. The Joule heating depends on the distribution of the current density and the electrical conductivity of the materials, so the Joule heating of the electrode and the ingot are smaller than the Joule heating of the slag bath. Because of the maximum current density near the electrode corner in

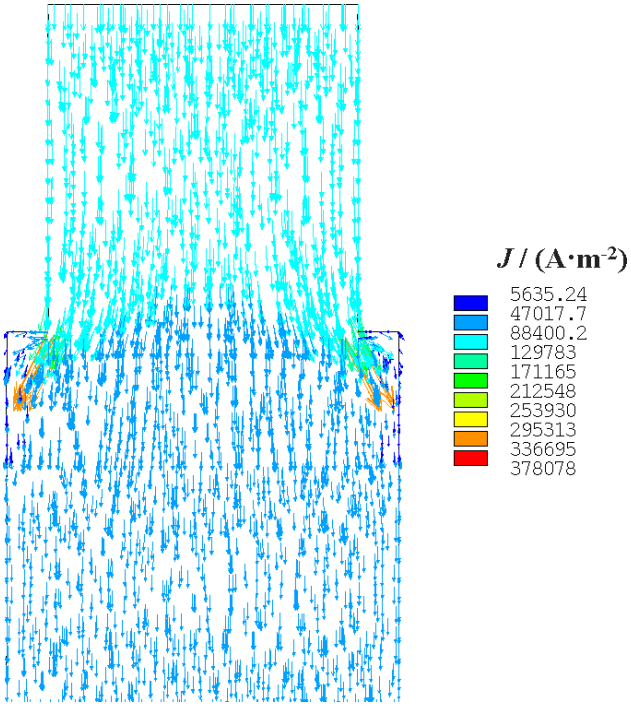

Figure 5: The current density distribution of longitudinal section of the ESRW

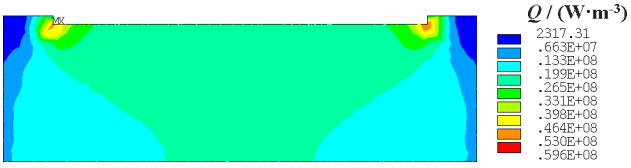

Figure 6: The Joule heat distribution in the slag bath

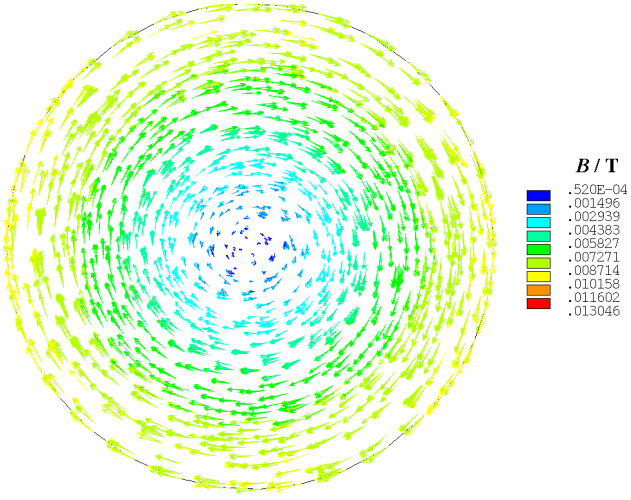

Figure 7: The magnetic flux density distribution of cross section in the slag bath

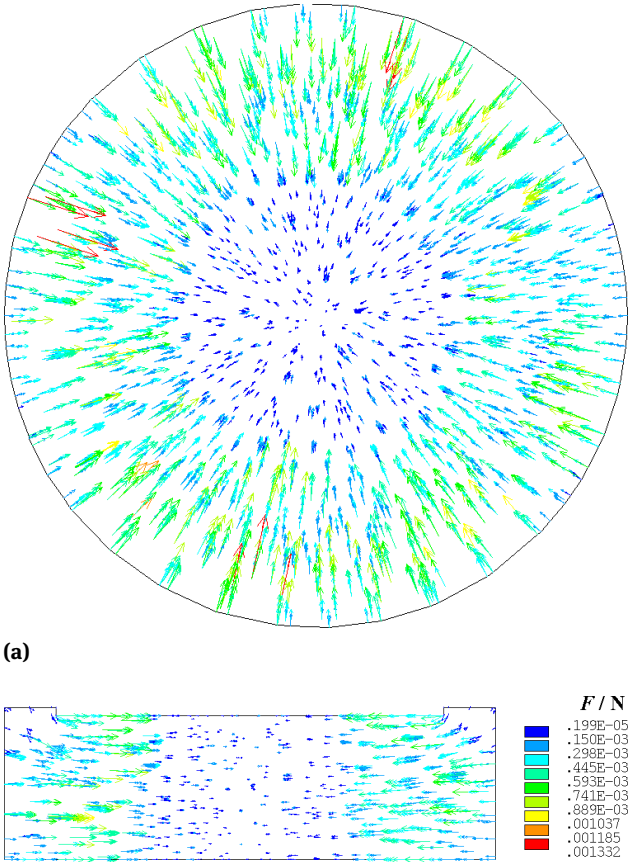

Figure 8: The electromagnetic force distribution in (a) the cross-section and (b) the longitudinal section of the slag bath

the slag bath, the Joule heat of the electrode corner in the slag bath has the highest value of 0.596×10^{8} W·m^{-3}.

Figure 7 shows the magnetic flux density distribution of cross section in the slag bath. The direction of the magnetic flux density is tangential to the slag bath and has a clockwise rotation. Its direction and the direction of the current density correspond to the right-hand rule. The magnetic flux density is the smallest at the center of the slag bath, where the value is 0.52×10^{-4} T. It is noted that the magnetic flux density increases from the center to the periphery in the slag bath. The maximum value is 0.013 T.

Figure 8 shows the electromagnetic force distribution in the cross-section and the longitudinal section of the slag bath in the ESRW system. Figure 8 (a) shows that the electromagnetic force points to the center of the slag bath. Figure 8 (b) shows that the electromagnetic force is tangential direction to the current density and follows the left-hand rule for the direction of the current density and the direction of the magnetic flux density. The electromagnetic force is divided into two components in the axial and radial directions near the electrode corner of the

slag pool. The electromagnetic force becomes smaller and smaller in the radial direction, reaching a minimum value of 0.199×10^{-5} N. The maximum value near the electrode corner is 0.001 N.

3.2 Velocity field

Figure 9 shows the velocity distribution of the longitudinal section of the slag bath in the ESRW system. There are two pairs of vortices, a pair of large ones at the center of the slag bath under the electrode and another pair of small ones near the electrode corner. The large vortices have a counterclockwise rotation due to the influence of the Lorentz force and the metal droplets dripping traction. The small vortices have a clockwise rotation due to the effects of buoyancy and temperature gradients. The calculated vortices are 0 to 0.08 $m\cdot s^{-1}$ in the slag bath. The maximum value and the minimum value occur close to the central axis of the slag bath and near the center of the vortices.

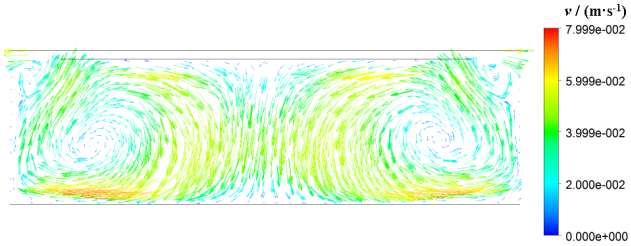

Figure 9: The velocity distribution of longitudinal section of the slag bath

3.3 Temperature field and shape of the molten-metal pool

Figure 10 shows the temperature distribution of the longitudinal section in the ESRW system. Due to uneven distribution of the current density in the slag bath and the flow of the slag, the temperature field is distributed unevenly in the slag bath. There are two high temperature zones (1990 K) that are found on both sides of the central line in the slag bath. This is mainly due to two factors. First, the speed of the center of the large vortices is small in the slag bath, so the slag will not spread out and lose its heat. Second, the metal droplets absorb the heat of the slag in the slag pool, so the high temperature zones of the slag bath move to the nearby center of the vortices. The temperature closer to the electrode is lower than in the slag bath. Because the

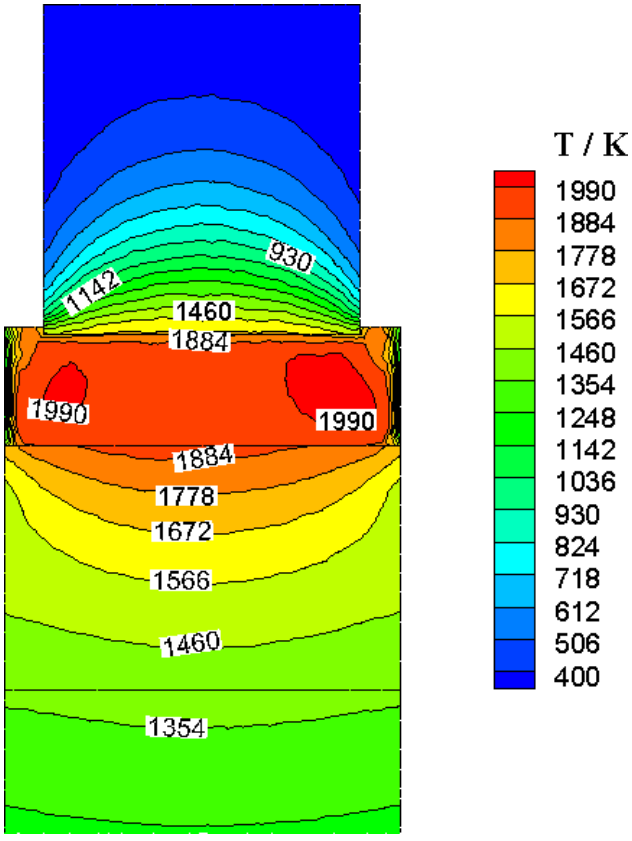

Figure 10: The temperature distribution of longitudinal section of the ESRW system

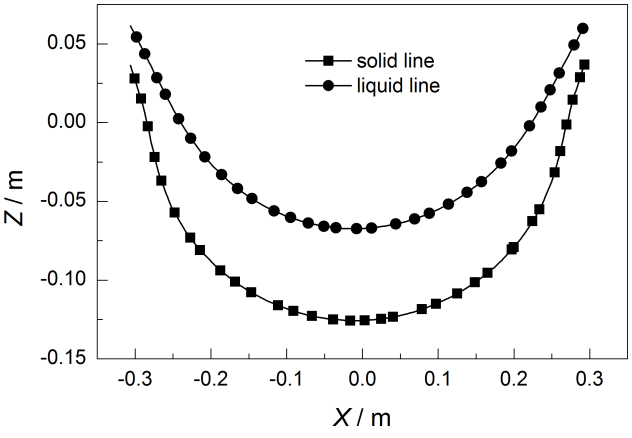

Figure 11: The shape of metal pool in longitudinal section of the ESRW process

slag pool is cooled by the mould, the temperature gradient is large at the sidewall of slag.

Figure 11 shows the shape of the molten-metal pool for the temperature field in the ESRW system. Figure 10 and 11 show that the metal droplets carry a large amount of heat into the molten-metal pool, the temperature is high in the middle of ingot. The ingot cools near the mould, so the tem-

perature gradient of ingot surface increasing distance from the center, and the faster heat transfer leads to lower the temperature. The molten-metal pool has the appearance of a "bowl". The ingot is air cooling outside the mould, so the temperature gradient of the ingot is small. Figure 11 shows that the depth of the liquidus line is 0.12 m and the depth of solidus line is 0.20 m. The maximum depth of the two-phase region is 0.08 m.

The experiment using the ESRW process (Current amplitude 16500 A, Frequency 50 Hz, Electrode immersed depth 0.01 m, slag height 0.18 m) for producing an ingot of 9Cr3Mo roller was done by using the slag system with 60% CaF_2, 20% CaO, and 20% Al_2O_3 and the technological parameters listed in Table 1. It was very difficult to measure the surface temperature of the ingot in the mould, so the surface temperature of the ingot outside mould was measured by an HY63 infrared thermometer. Figure 12 shows the temperature-measured position on the ingot surface. Figure 13 shows the comparison of the numerical simulation values and the actual measured values of the surface temperature of the ingot, which shows that the calculated values are in good agreement with the measured values.

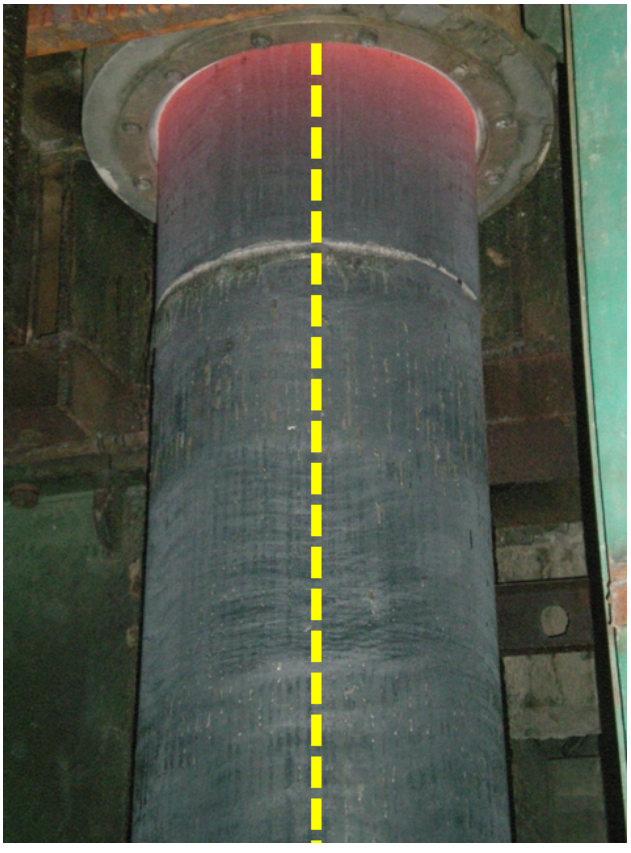

Figure 12: Line of the ingot surface for measuring temperature

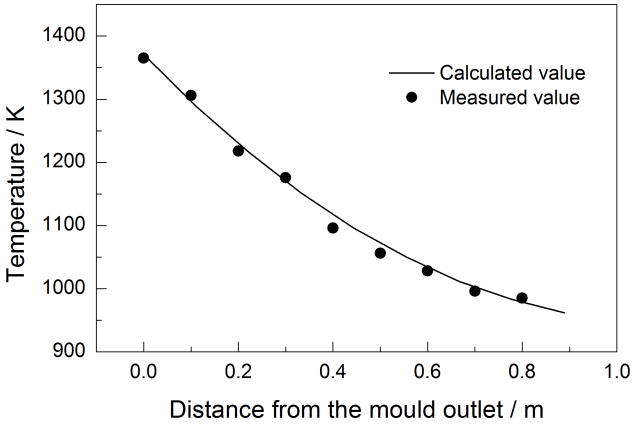

Figure 13: The calculated temperature and the measured temperature of the ingot surface below the mould outlet

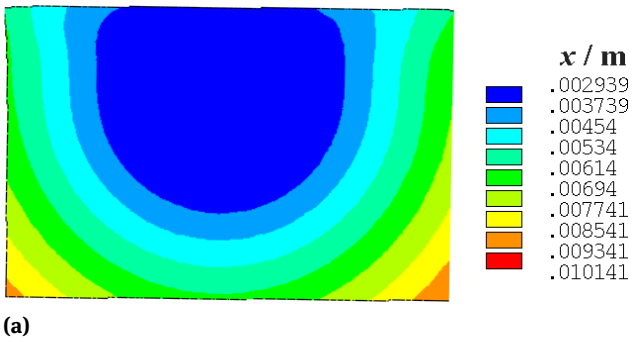

(a)

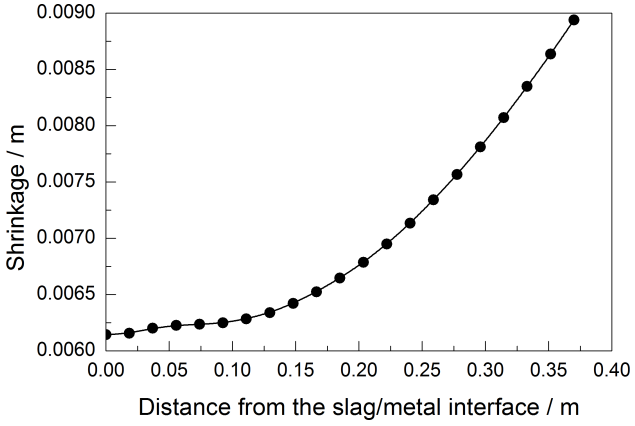

(b)

Figure 14: (a) The shrinkage displacement of longitudinal section of the ingot and (b) ingot shrinkage curve in the mould

3.4 Numerical simulation and model validation of ingot shrinkage

Figure 14(a) shows the shrinkage displacement of the longitudinal section of the ingot in the mould. Figure 14(b) is a shrinkage curve drawn from the shrinkage displacement of the left side surface of the ingot. Figure 14(a) shows that the shrinkage displacement of the ingot increases gradu-

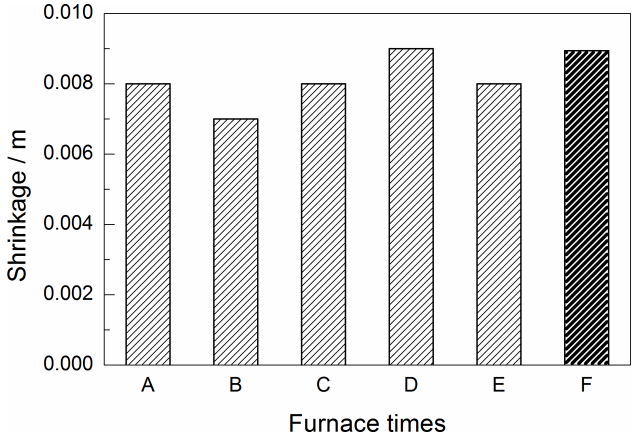

Figure 15: The comparison between the measured values (A, B, C, D, E) of the shrinkage displacement of the ingot at the mould outlet for different furnace times and calculated value (F) of the ESRW

ally from the center of ingot to the surface. Figure 14(b) shows that the variation of the shrinkage displacement between the slag/metal interface and the mould outlet is 0.0028 m. Figures 14(a) and 14(b) show that as the distance from the mould outlet decreases, the shrinkage displacement of the ingot increase. The maximum value of the shrinkage displacement is about 0.00894 m at the mould outlet. Due to cooling effect of the mould, the surface temperature of the ingot is lower than the center, so the shrinkage in the boundary layers is greatest. Closer to the ingot axis, the change of shrinkage displacement is considerably slower. This results from the variation of the thermal flux. On account of rapid shrinkage at the corners of ingot, the gap increases sharply, and hence the thermal flux is sharply reduced. In turn, it slows the shrinkage and the gap begins to slowly decrease in mold cross section.

To verify the accuracy of the simulation results of ingot shrinkage, shrinkage displacement of five electroslag ingot under the same process conditions as Table 1 were measured. Figure 15 shows the comparison between the measured values (A, B, C, D, E) of the shrinkage displacement of the ingot at the mould outlet for different furnace times and the calculated value (F) of the ESRW (Current amplitude 16500 A, Frequency 50 Hz, Electrode immersed depth 0.01 m, slag height 0.18 m) for the same working conditions. The calculated value is in good agreement with the measured values.

4 Conclusions

(1) The potential drop is the greatest in the slag bath. The maximum values of the current density, the Joule heating, and the electromagnetic force are found near the electrode corner in the slag bath. The magnetic flux density increases from the center to the periphery in the slag bath.

(2) The velocity field has two pairs of vortices in the slag pool, a large pair with counterclockwise rotation, and another small pair with clockwise rotation. There are two high temperature zones in the slag bath, which are distributed on both sides of the central line in the slag bath.

(3) The shrinkage displacement of the ingot increases gradually from the center of the ingot to the surface. As the distance from the mould outlet decreases, the shrinkage displacement of ingot increases. The maximum shrinkage displacement is at the mould outlet, and the value was 0.0089 m

Acknowledgement: This work is supported by National Natural Science Foundation of China (No.51604149, No.U1560203). Also, this project is supported by national key laboratory of marine engineering of China (No. SKLMEA-USTL-201707).

References

[1] Z.B. Li, China Foundry, 1 (2004) 7-16.
[2] S.W. Cai, T.M. Wang, J. Li, J.J. Xu, Y.Y. Du, Z.Q. Cao, and T.J. Li, Special Casting & Nonferrous Alloys, 8 (2009) 709-712.
[3] X.M. Zang, Z.H. Jiang, L. Medovar, and H.L. Jiang, J. Mat. Metall., 10S1 (2011) 81-85.
[4] L. Fubin, Z. Ximin, J. Zhouhua, G. Xin, and Y. Man, J. Univ. Sci. Technol. B, 4 (2012) 303-311.
[5] A. Kharicha, A. Ludwig, and M. Wu, Mater. Sci. Eng., A, 6 (2005) 129-134.
[6] E. K. Sibaki, A. Kharicha, M. Wu, A. Ludwig, H. Holzgruber, B. Ofner, and M. Ramprecht, *Proceedings of the* 2013 *International Symposium on Liquid Metal Processing & Casting*, September 22-25, 2013, Austin, Texas, TMS, USA, (2013) , pp. 13-19.
[7] B.K. Li, F. Wang, and F. Tsukihashi, ISIJ Int., 7 (2012) 1289-1295.
[8] X.H. Wang and Y. Li, Metall. Mater. Trans. B, 2 (2015) 800-812.
[9] F. Wang, Y.C. Lou, R. Chen, Z.W. Song, and Q. Wang, *TMS* 2015 *144th Annual Meeting & Exhibition: Supplemental Proceedings*, March 15-19, 2015, Orlando, Florida, TMS, USA, (2015), pp. 783-790.
[10] F. Wang, Q. Wang, Y.C. Lou, R. Chen, Z.W. Song, and B.K. Li, JOM, 1 (2016) 410-420.
[11] Q. Wang, Z. He, B.K. Li, and F. Tsukihashi, Metall. Mater. Trans. B, 6 (2014) 2425-2441.
[12] Q. Wang, W.J. Rong, and B.K. Li, JOM, 11 (2015) 2705-2713.
[13] C.S. Li and B.G. Thomas, Metall. Mater. Trans. B, 6 (2004) 827-834.
[14] S. Koric and B.G. Thomas, J. Mater. Process. Tech., 1 (2008) 408-418.

[15] B.F. Wang, G. Ding, and J.W. Zhao, Special Steel, 2(2005) 38-40.
[16] W.H. Wang, Y. Liu, and W.J. Wang, Iron Steel Res., 6 (2014) 26-29.
[17] T.M. Wang, S.W. Cai, J. Li and T.J. Li, China Foundry, 1 (2010) 61-67.
[18] S.W. Cai, T.M. Wang, J.J. Xu, J. Li, Z.Q. Cao, and T.J. Li, Mater. Res. Innov., 1 (2011) 29-35.
[19] B. E. Launder and D. B. Spading, Mathematical Models of Turbulence, Academic Press, London, (1972).
[20] E.G. Wang, J.C. He, Z.K. Yang, H.G. Chen, J. Northeast. Univ., 6(1998) 555-557.
[21] M. Choudhary and J. Szekely, Metall. Trans. B, 3 (1980) 439-453.